https://doi.org/10.5194/egusphere-2026-4775
Preprint. Discussion started: 21 August 2026

Wind-Informed Bayesian Classification of L-band SAR Imagery for Sea Ice and Open Water Separation

Truls Karlsen[1], Johannes Lohse[2, 1], Randall Scharien[3], Malin Johansson[1], and Anthony P. Doulgeris[1]

[1]Department of Physics and Technology, UiT The Arctic University of Norway, Tromsø, Norway
[2]Australian Antarctic Program Partnership, Institute for Marine and Antarctic Studies, University of Tasmania, Nipaluna / Hobart, Tasmania
[3]Department of Geography, University of Victoria, Victoria, BC, Canada

Correspondence: Truls Karlsen (truls.t.karlsen@uit.no)

Abstract. We present a robust, incidence angle (IA) and wind speed aware model for separating sea ice from open water and providing high resolution sea ice concentration (SIC) estimates from L-band synthetic aperture radar (SAR) imagery, with potential climate study and operational benefits. By treating open water as a wind speed-dependent class in an established IA-aware Bayesian maximum likelihood ice type classifier, we account for the wind-driven open water backscatter variability by using external wind information. This method circumvents the need for the extensive training datasets or accurate geophysical model functions (GMFs) typically required by established C-band ice/water separation algorithms. To demonstrate this approach, we utilize wide-swath dual-polarized (HH/HV) L-band SAR data from the ALOS-2 mission. The proposed method provides high accuracy during the challenging melt period, achieving high Matthews Correlation Coefficient (MCC) scores (MCC>0.800), and consistently outperforms passive microwave radiometer (PMW) products during this period. During winter conditions, weak sea ice backscatter and system noise limitations hindered reliable ice/water separation (MCC=0.506). We compare our proposed method to a baseline model without incorporated external wind information, and find that the wind-informed classifier achieves consistently higher classification accuracies. Our results demonstrate that integrating external wind data allows for robust, high resolution ice/water separation in L-band SAR imagery during melting conditions based purely on backscatter intensity, removing the need for computationally heavy textural features.

1 Introduction

Sea ice concentration (SIC) is a key variable for climate monitoring and for operational applications such as navigation and route planning in polar waters (Lavergne et al., 2022). Although passive microwave radiometers (PMW) provide long-term, all-weather SIC records at regional to global scales, their coarse spatial resolution limits the representation of fine-scale ice features, while retrieval uncertainties increase during melt conditions as wet snow and melt ponds affects the microwave signature of sea ice (SI) (Comiso and Parkinson, 2008; Kern et al., 2020). Synthetic aperture radar (SAR) therefore provides an important complementary capability for high-resolution mapping of SI and open water (OW) in polar regions. While ice services currently rely on manual interpretation of the SAR imagery by trained experts, this approach is both time-consuming and subject to human bias, driving continued research into automated alternatives. Historically, these efforts have focused

https://doi.org/10.5194/egusphere-2026-4775
Preprint. Discussion started: 21 August 2026

on C-band SAR due to the vast operational data archives provided by missions such as Sentinel-1, RADARSAT-2, and the RADARSAT Constellation Mission (RCM), e.g., (Wang et al., 2016; Wang and Scott, 2017; Komarov and Buehner, 2020; Karvonen et al., 2020; Radhakrishnan et al., 2021; Wang et al., 2023; Wulf et al., 2024; Rusin et al., 2025; Wulf et al., 2026). However, the recent launch and upcoming deployment of next-generation L-band SAR missions — such as ALOS-4, NISAR and ROSE-L — highlight the growing importance of developing efficient and reliable classification frameworks tailored to wide-swath L-band data.

Ice/water classification in SAR imagery is particularly challenging due to the high variability of OW backscatter, which is driven by surface roughness from local wind conditions (Fu and Holt, 1983). Additionally, SI backscatter signatures are not only affected by the small- and large-scale surface roughness of the ice, but also by seasonal cycles, snow cover, salinity, and internal ice and snow volume structures (Onstott and Gogineni, 1985; Barber et al., 2001). While multi-temporal training sets for different SI types can mitigate seasonal variability, the sensitivity of OW backscatter to surface wind conditions requires additional information beyond single-pixel backscatter intensity. Current approaches to address these challenges include: (a) spatial texture features or Convolutional Neural Networks (CNNs) (Karvonen, 2013; Wang et al., 2016; Wang and Scott, 2017; Lohse et al., 2021; Rusin et al., 2025), (b) multi-sensor data fusion (Karvonen, 2014; Radhakrishnan et al., 2021; Wang et al., 2023; Wulf et al., 2024, 2026), and (c) the integration of external meteorological data (Komarov and Buehner, 2017, 2020). Because of the larger abundance of C-band data compared to L-band data, most of this work until now has been focused on C-band SAR.

Previous L-band studies (Wakabayashi et al., 2004; Wakabayashi and Sakai, 2010; Casey et al., 2016; Aldenhoff et al., 2018; Johansson et al., 2018; Karvonen et al., 2020; Mahmud et al., 2022) have highlighted challenges for the operational use of L-band SAR, with the lack of openly available wide-swath SAR data being one of the major challenges. While fully polarimetric L-band data has been shown to successfully separate SI and OW based on polarimetric entropy (Wakabayashi et al., 2004; Wakabayashi and Sakai, 2010) or the ratio between the co-polarized backscatter channels (Johansson et al., 2017, 2018), such acquisitions lack the swath width necessary for large-scale monitoring. Conversely, dual-polarimetric wide-swath studies emphasize that texture features are essential for successful ice/water separation (Aldenhoff et al., 2018; Karvonen et al., 2020; Mahmud et al., 2022); however, these features are computationally expensive and often necessitate large processing windows that degrade the effective spatial resolution of the resulting SI maps (Lohse et al., 2021). CNNs offer an alternative by inherently capturing contextual image information, but their application to L-band SAR is constrained by the scarcity of high-quality L-band training data. Existing operational ice charts, primarily derived from C-band interpretations, lack sufficient temporal overlap with L-band acquisitions to serve as reliable training labels.

To circumvent these limitations — specifically the computational burden of texture analysis and the lack of sufficient L-band training data for CNNs — we incorporate modeled meteorological wind data into the classification process to resolve overlapping backscatter signatures between SI and OW. The inclusion of wind data has been successfully demonstrated for C-band by (Komarov and Buehner, 2017, 2020), who used Geophysical Model Functions (GMFs) to derive wind speed directly from SAR backscatter intensity and identify anomalies against numerical weather models; pixels with large anomalies were then classified as SI. For L-band, however, operational GMFs that simultaneously cover HH and HV polarizations are currently lacking.

https://doi.org/10.5194/egusphere-2026-4775
Preprint. Discussion started: 21 August 2026

We therefore introduce a method that incorporates model-derived wind speeds directly into a Bayesian ice-type classifier introduced in (Lohse et al., 2020), where the surface-dependent incidence angle (IA) dependency is treated as an inherent class property. In our framework, wind-driven backscatter variability is accounted for by utilizing wind-speed-dependent probability density functions (PDFs). To achieve this, we derive PDFs empirically from a large archive of L-band SAR data co-located with in-situ meteorological buoy measurements of wind speed and direction. This enables the conditional selection of OW class parameters based on modeled wind data during forward classification of new L-band images, ultimately providing a robust, texturally independent framework for high-resolution ice/water separation, with the estimation of SIC as the end goal.

2 Study area and data

2.1 Study area

In this study, we make use of two SAR datasets; one for estimating SI model parameters and evaluation of the classifier, and another for estimating OW model parameters. The study area for the first dataset covers four test sites in the Arctic: the Fram Strait (FS), the Canadian Arctic Archipelago (CAA), the Arctic Ocean North of Greenland (NOG), and the North-east coast of Canada (NEC). Scene outlines of the SAR imagery used from each region are shown in Figure 1. General SI conditions in the dataset ranged from high SIC (predominantly SI, with smaller OW features like open leads), medium SIC (a mixture of landfast ice, small and large floes, brash ice, leads, and larger areas of OW), to low SIC (mainly OW, with some ice features present). The second dataset consists of L-band SAR imagery overlapping fixed meteorological buoys, the locations of which are shown in Figure 2 (a). This dataset is used to assess the influence of wind conditions on L-band OW backscatter.

2.2 Remote sensing data

2.2.1 ALOS-2

A total of 7923 ALOS-2 ScanSAR 14 MHz scenes in Level 2.2 (L2.2) format are used in this study. We use 7882 ALOS-2 scenes overlapping 92 fixed meteorological buoys, the locations of which are shown in Figure 2 (a), to assess the influence of wind speed on L-band OW backscatter. The remaining 41 ALOS-2 images are used for generating SI training ROIs, as well as validation ROIs for both SI and OW, and are collected across the four test sites described in Section 2.1.

To capture L-band backscatter at the full range of IAs for a broad range of wind speeds, significantly more images are used in the first dataset which overlaps with the buoy locations. Only one point (around a buoy location) in each of these images is sampled, whereas the 41 scenes used for SI training and SI/OW validation include multiple ROIs within each image (see section 2.3 for further details).

Sensor specifics for the ALOS-2 ScanSAR 14 MHz mode are presented in Table 1. We use dual-polarized data for separating SI from OW, and a combination of dual- and single-polarized data to assess the influence of wind speed on L-band OW backscatter. The L2.2 data is provided as map-projected imagery calibrated to γ^0, which we convert to σ^0 as this calibration level is most commonly used in SAR SI research (e.g. (Isoguchi and Shimada, 2009; Komarov and Buehner, 2017; Lohse et al.,

https://doi.org/10.5194/egusphere-2026-4775
Preprint. Discussion started: 21 August 2026

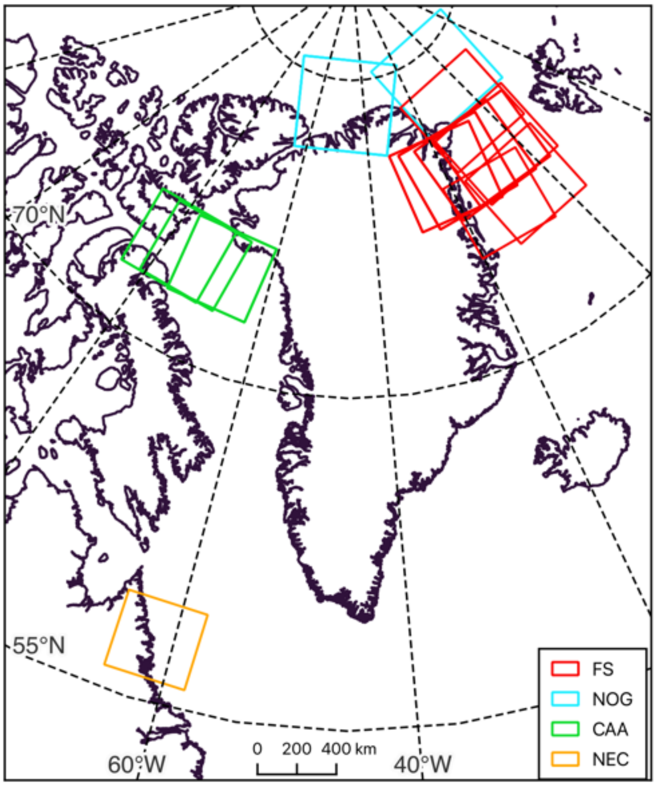

Figure 1. Outlines of the ALOS-2 scenes used to extract regions of interest (ROIs) for SI and OW. The four test sites are indicated with different colored outlines, red (Fram Strait), blue (North of Greenland), green (Canadian Arctic Archipelago), and orange (North-east coast of Canada). Free vector and raster map data @ naturalearthdata.com

2020; Karvonen et al., 2020; Mahmud et al., 2020; Geldsetzer and Howell, 2023; Karlsen et al., 2024)). Significant scalloping is present in the imagery, which we aim to mitigate by applying a Gaussian notch reject filter in the frequency domain. To do so, we rotate the images to an approximate radar coordinate system (range $\times$ azimuth), to easily apply the notch filter in azimuthal direction. This reduces the scalloping effect, at the cost of a slight blurring of the images (Gonzalez and Woods, 2018). As the L2.2 data is already map-projected, true multi-looking is not straight forward. Hence, we approximate multi-looking by applying a spatial moving average filter on the imagery in the approximated radar coordinate system. We use a 12×12 window, yielding a pixel spacing of 300 m which matches the spatial resolution of the Sentinel-3 (S3) optical imagery (see Section 2.2.2). The imagery is then rotated back to the original map projected coordinate system.

Table 1. Specifics of the ALOS-2 ScanSAR 14 MHz mode

Swath width	Pixel spacing	Polarization	IA range	NESZ [1]
350 km	25 m	HH / HH + HV	25° - 50°	-30.0 and -32.5 dB [2]

https://doi.org/10.5194/egusphere-2026-4775
Preprint. Discussion started: 21 August 2026

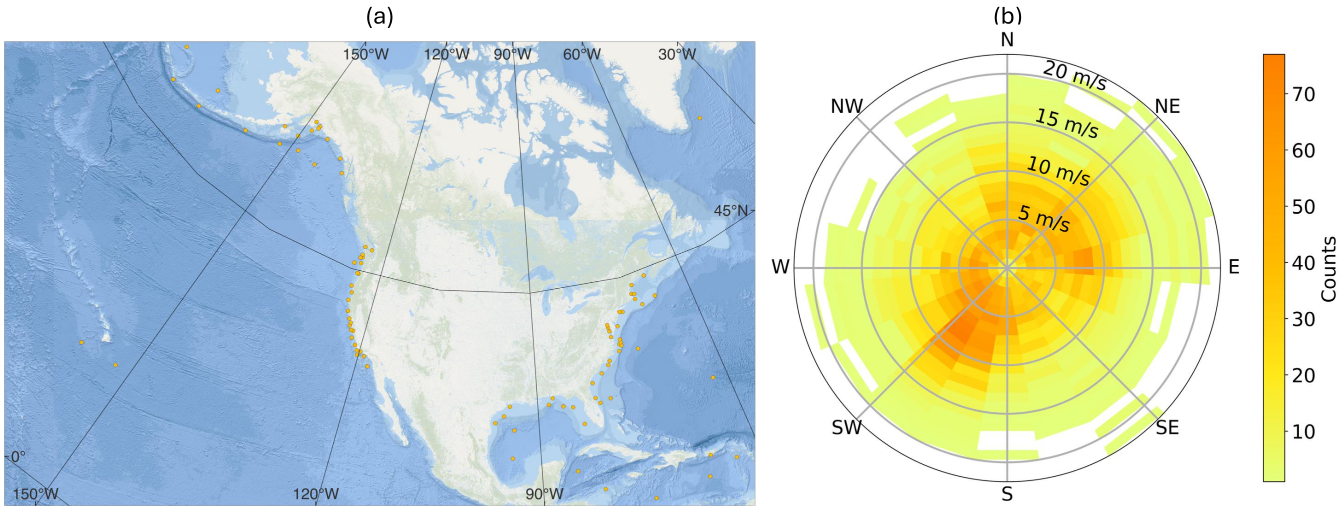

Figure 2. Location of the 92 meteorological buoys used for reference ocean wind data indicated by orange dots (a) and heatmap of obtained wind conditions during coinciding ALOS-2 image acquisitions from 7882 images (b).

2.2.2 Optical imagery

Optical imagery from the Sentinel-2 (S2) and S3 missions was used to support ROI selection in the SAR imagery; the ROIs are then used for estimating SI model parameters and validation of the ice/water classifier on the first ALOS-2 dataset. We also used the optical imagery to help determine seasonal stages, e.g., by assessing the presence of melt ponds, bare ice, or snow cover, and to aid in visual inspection of the results. Further details on the seasonal stages are presented in Section 2.3.The difference in acquisition time between the SAR and optical imagery ranged from 8 seconds to 7.7 hours. We did not set a strict threshold for a maximum time difference, but rather visually inspected overlapping images to assess whether ice drift between the acquisitions still allowed us to clearly identify the same individual floes, leads, and SI types in both images. We also manually screened optical images for the presence of clouds, ensuring that small cloud-free regions of otherwise cloud-covered images could be utilized, which enabled us to use a larger total number of overlapping images (71 image mosaics in total).

The S3 mission consists of two identical satellites (S3-A and -B) in the same orbit, which among other sensors carry the Ocean and Land Colour Instrument (OLCI), providing optical data with a spatial resolution of 300 m. We use the visual bands 4, 6, and 8 to generate true-color composites (TCCs). Although S3 has a coarser spatial resolution than other freely available optical data sources (e.g. S2 and Landsat 8/9), the frequent revisit times and large spatial coverage enabled us to reliably find overlapping ALOS-2 and S3 scenes with small differences in acquisition time. Additionally, the S3 data coverage extends

[1]Noise equivalent sigma zero
[2]For HH and HV respectively

https://doi.org/10.5194/egusphere-2026-4775
Preprint. Discussion started: 21 August 2026

further north than the S2 coverage, which was necessary for coverage over the NOG test site. We used 41 S3 mosaics in this study, with one mosaic corresponding to each SAR image.

When available, we used optical data from the S2 mission, which consists of three identical satellites (S2-A, -B, and -C) in the same orbit. The coverage of S2 extends from 84°S to 84°N[3]. For our purpose, only the red, green, and blue channels (bands 2, 3 and, 4), provided at 10 m spatial resolution, were used to create a TCC. Whilst the high spatial resolution enabled the separation of small regions of ice and water, the limited temporal and spatial coverage of S2 made finding good match-ups with the ALOS-2 data challenging. As such, only 30 of our SAR scenes had usable overlapping S2 imagery. These 30 S2 mosaics were used in addition to the S3 mosaics described earlier.

2.3 ROI selection

Using the first ALOS-2 dataset described in Section 2.1, we select ROIs for SI and OW by visual assessment and interpretation of overlapping optical and SAR imagery. While the SI class parameters (see Section 3.1) for the classifier used in this study are estimated from these ROIs, the OW class parameters are estimated from the second ALOS-2 dataset that overlaps with the meteorological buoys (see Section 2.4). We split the SI ROIs on a whole-image basis into a training and a validation set, while all the OW ROIs are used for validation. To ensure that our evaluation covers a wide range of wind conditions at a broad range of IAs, the amount of evaluation ROIs/pixels for OW is larger than for SI. Table 2 shows an overview of the final number of training and validation images, ROIs, and pixels for each class. Note that the SI ROIs (both training and validation) are further divided into two different SI types with four seasonal stages each. Below, we describe the reasoning behind this split.

SI backscatter signatures vary significantly for different ice characteristics, with particular influence from SI surface roughness at small (i.e. wavelength) scales and large scales, like deformation in pressure ridges or rubble fields. We manually group the SI ROIs into level and deformed ice (LI and DI, respectively), following the descriptions given in (Karlsen et al., 2024; Lohse et al., 2024). DI is ice that has undergone mechanical deformation, and consists of a mixture of first- and multi-year ice (FYI and MYI respectively), while LI is smooth, undeformed ice which consists primarily of FYI. The large-scale deformation features of the DI lead to a backscatter signature that is dominated by random tilt angles and multiple reflections. This results in high backscatter intensity in both the co- and cross-polarized channels. LI on the other hand has a relatively smooth surface relative to the radar wavelength, with no large-scale tilt angles, resulting in predominantly specular surface scattering. This leads to a weaker backscatter signal, particularly for the cross-polarized channel. Furthermore, the differences in dominant scattering mechanisms for LI and DI lead to differences in IA dependency, with LI typically displaying a stronger decay with IA than DI (Karlsen et al., 2024).

Note that, while the distinction between LI and DI is needed for accurate class representation in our classifier (Section 3.1), the goal of this study is the separation of OW and SI in general to derive high-resolution SIC. Hence, after classification and before evaluation, LI and DI were merged to one single SI class.

Finally, the backscatter signatures of SI also has a seasonal component (Barber et al., 2001). During the winter season, the snowpack is dry, and much of the scattering is assumed to occur at the ice/snow interface or within the SI at L-band (Karlsen

[3]https://www.esa.int/Applications/Observing_the_Earth/Copernicus/Sentinel-2/Facts_and_figures, accessed 26-11-2025

https://doi.org/10.5194/egusphere-2026-4775
Preprint. Discussion started: 21 August 2026

et al., 2024). During the melt season, the presence of liquid water within the snowpack, and melt ponds as the melt season progresses, drastically change the backscatter signatures. The melt season can be further divided into the following seasonal stages; early melt, melt onset, ponding, and drainage. Following the drainage season, freeze-up occurs when new ice starts forming in the autumn (Barber et al., 2001). As the L-band backscatter signatures during early melt are similar to the winter season (Mahmud et al., 2020), we made no distinction between the two in this study. We could not find sufficient match-ups between ALOS-2 and optical imagery during the freeze-up period, so this seasonal stage was omitted as well. Using the overlapping optical imagery to identify features such as melt ponds and bare ice, we manually assign a seasonal stage to each SAR image.

Table 2. Number of images, ROIs and pixels used for estimating the SI parameters and validating the model performance.

		Winter	Melt onset	Ponding	Drainage	Total
# of images	Train	7	2	2	3	14
	Validate	7	3	8	9	27
# of ROIs	Train (LI)	97	81	49	72	299
	Train (DI)	585	239	68	121	1013
	Validate (SI)	96	32	121	136	385
	Validate (OW)	71	53	153	165	442
# of pixels	Train (LI)	12318	4634	6158	13679	36789
	Train (DI)	113641	28713	13578	11967	167899
	Validate (SI)	33573	16696	55846	25432	131548
	Validate (OW)	16098	57276	160409	19869	253652

2.4 Wind data

The goal of this study is the incorporation of wind information in a Bayesian maximum likelihood classifier to resolve OW backscatter ambiguities. For this purpose, the relationship between OW L-band backscatter and wind speed as a function of IA needs to be established at a range of wind speeds. Additionally, the corresponding wind field of an ALOS-2 scene is required during forward classification. For these two components, we make use of two separate datasets; 1) ocean meteorological buoys with overlapping ALOS-2 imagery for establishing the relationship between L-band OW backscatter and wind speed, 2) reanalysis data for forward classification.

https://doi.org/10.5194/egusphere-2026-4775
Preprint. Discussion started: 21 August 2026

2.4.1 Meteorological buoys

For characterizing the influence of wind on OW backscatter in L-band SAR imagery, we used 7882 of the ALOS-2 ScanSAR scenes overlapping 92 fixed national data buoy center (NDBC) [4] meteorological buoys located mainly along the US coast (Figure 2 (a)). The NDBC buoys measure wind speed and direction, as well as other meteorological and oceanographic parameters, with sampling intervals ranging from 10 minutes to one hour, and anemometer heights ranging from 2.7 m to 5.7 m. A maximum time separation of 30 minutes was allowed between a SAR acquisition and a NDBC buoy measurement. The wind speeds are quality controlled and checked before release, and erroneous values are flagged (Center, 2023). The overlapping ALOS-2 data consisted of 2830 single-polarized scenes (HH) and 5052 dual-polarized scenes (HH+HV). We extracted the mean SAR backscatter and IA around the location of each NDBC buoy. For a consistent dataset, we converted the NDBC buoy wind speed measurements to the standard reference height of 10 m above the surface using the Power law method described in (Hsu et al., 1994)

$$u_{10} = u_1 \left(\frac{10}{z_1}\right)^{0.11} \tag{1}$$

where z_1 is the height above sea level of the wind speed measurement u_1.

A heatmap showing the distribution of obtained wind conditions is shown in Figure 2 (b). In the range 0-10 m/s, the coverage is dense across all wind directions. The coverage in the range 10-15 m/s is sparser, with an over-representation in the S-SW and N-NE wind directions. In the range 15-21 m/s, the data are sparse in all directions. No data were obtained from higher wind speeds ($u_1 > 21$ m/s). The full range of wind speeds included in this study is thus 0 - 21 m/s. An overview of the overlapping L-band backscatter and NDBC buoy wind speeds as a function of IA is shown in Figure 3, illustrating the influence of wind speed on L-band OW backscatter intensity, as well as its strong IA dependency. These effects are most notable for the HH-channel.

2.4.2 Reanalysis data

The forward classification of new SAR data into SI and OW requires coincident wind speed information. Here we use wind speed from the Copernicus Arctic Regional Reanalysis (CARRA) west-domain [5]. It provides climate reanalysis data at a 2.5 km horizontal resolution, delivered at 3 hour intervals, with the wind data provided at the standard reference height of 10 m (Schyberg et al., 2020; Køltzow et al., 2022). With the higher spatial resolution of CARRA compared to previous reanalysis datasets (e.g., 31 km for ERA5), local wind conditions are captured at a scale more appropriate for SAR images. In order to use the CARRA wind speed data in conjunction with the SAR data, we up-sampled to the same spatial resolution as the spatially averaged ALOS-2 data (300 × 300 m) using a nearest-neighbor interpolation.

[4] https://www.ndbc.noaa.gov, accessed: 17-09-2025

[5] https://climate.copernicus.eu/copernicus-arctic-regional-reanalysis-service, accessed: 28-05-2025

https://doi.org/10.5194/egusphere-2026-4775
Preprint. Discussion started: 21 August 2026

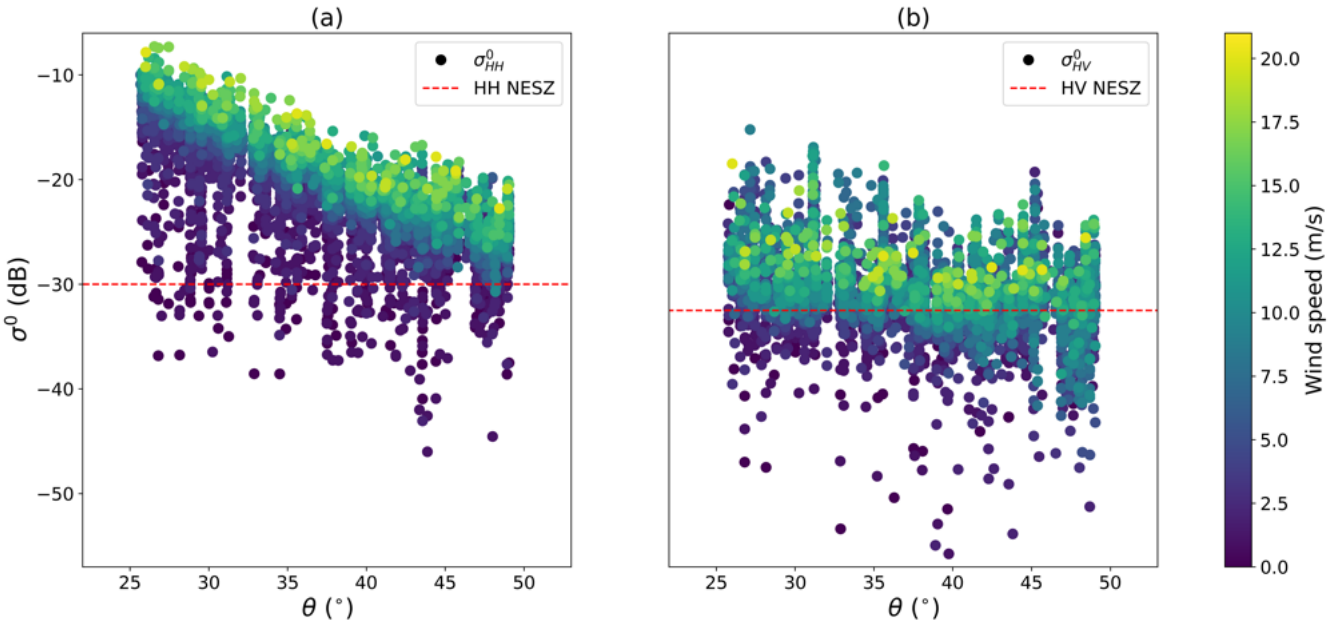

Figure 3. L-band OW HH- (a) and HV-channel backscatter as a function of IA (θ), color-coded by wind speed. The red dashed line indicates the channel-specific NESZ. The data clearly shows how OW backscatter is affected by both wind speed and IA, with higher wind speeds leading to stronger backscatter, while the backscatter intensity is inversely proportional to IA. These effects are more strongly pronounced in the HH-channel (a) than in the HV-channel (b). Maps were created using the ESRI Ocean basemap.

2.5 Comparison dataset

2.5.1 Sea ice concentration from passive microwave radiometers

In order to assess the performance of our SAR-derived SIC estimates against an independent dataset, we made comparisons to a SIC product provided by the University of Bremen, derived from the Advanced Microwave Scanning Radiometer (AMSR-2). The PMW SIC product is generated using the Arctic Radiation and Turbulence Interaction STudy (ARTIST) Sea Ice (ASI) algorithm, and is provided daily [6], with a pixel spacing of 6.25 km for the pan-Arctic product and 3.125 km for the regional product. To ensure consistency between our study sites, we used the pan-Arctic product. The ASI product is generated using the polarization difference of the 89 GHz channel brightness temperatures, which has a higher spatial resolution than the lower-frequency bands. While this channel produces results at a higher spatial resolution, it is more susceptible to atmospheric influences in the form of clouds and atmospheric water vapor. This is mitigated through filtering based on the lower resolution channels, which can lead to an overestimation of SIC along the ice edge (Spreen et al., 2008; Melsheimer and Spreen, 2019). Of note, the PMW SIC data is not included in this study as validation data, but rather to provide a general comparison of our SIC results to that of a widely-used, operational SIC product.

[6] https://seaice.uni-bremen.de/sea-ice-concentration/amsre-amsr2/, accessed 12-11-2025

https://doi.org/10.5194/egusphere-2026-4775
Preprint. Discussion started: 21 August 2026

3 Method

The novel approach presented in this study is the inclusion of the physical effect of wind speed on L-band SAR backscatter into an IA-aware Bayesian maximum likelihood classification algorithm (Lohse et al., 2020) to account for OW backscatter variability, with the separation of SI and OW from L-band SAR data as the end goal. We therefore start by giving an overview of the classifier that our method is based on. Following this, we give a description of the proposed method to incorporate wind speed, followed by a description of the design to validate the proposed method.

3.1 Incidence angle aware classifier

The classification algorithm we use was introduced in (Lohse et al., 2020) to separate different SI types. This method is based on modeling the PDF of a given class ω_i as a multi-variate Gaussian distribution, where the linear decay of backscatter intensity in the dB domain is accounted for by parameterizing the mean vector as a function of IA

$$\boldsymbol{\mu}_i(\theta) = \boldsymbol{a}_i \cdot \theta + \boldsymbol{b}_i \tag{2}$$

where $\boldsymbol{a}_i$ and $\boldsymbol{b}_i$ are the slope and intercept of class ω_i, and θ is the IA. For a dual-polarization SAR pixel in dB, $\boldsymbol{x} = [\sigma^0_{\mathrm{HH}}, \sigma^0_{\mathrm{HV}}]$, the class-conditional PDF is then given as

$$p_i(\boldsymbol{x}, \theta | \omega_i) = \frac{1}{2\pi |\boldsymbol{\Sigma}_i|^{\frac{1}{2}}} e^{-\frac{1}{2}(\boldsymbol{x} - \boldsymbol{\mu}_i(\theta))^T \boldsymbol{\Sigma}_i^{-1} (\boldsymbol{x} - \boldsymbol{\mu}_i(\theta))} \tag{3}$$

The classifier requires $\boldsymbol{a}_i$, $\boldsymbol{b}_i$, and $\boldsymbol{\Sigma}_i$ to be estimated from the training data for each class. Note that the covariance matrix $\boldsymbol{\Sigma}_i$ is now defined as the mean squared deviation of the backscatter intensity relative to the IA-dependent mean value.

3.1.1 Sea ice class parameter estimation

We estimate the SI class parameters ($\boldsymbol{a}_i$, $\boldsymbol{b}_i$, and $\boldsymbol{\Sigma}_i$) of LI and DI separately for each seasonal stage (winter, melt onset, ponding, and drainage). The slope $\boldsymbol{a}_i$ and intercept $\boldsymbol{b}_i$ are calculated using a simple linear regression (SLR) on all training data points corresponding to an ice type for a given season, e.g. DI during winter, with backscatter and IA as the dependent and independent variables, respectively. The covariance matrix $\boldsymbol{\Sigma}_i$ is then calculated as the mean squared deviation of the backscatter intensity relative to linear fit.

3.1.2 Open water class parameter estimation

Using the overlapping L-band SAR imagery and NDBC buoys described in Section 2.4.1, we estimate the OW class parameters per 1 m/s wind speed bin. Following the same procedure as for SI, the slope $\boldsymbol{a}_i$ and intercept $\boldsymbol{b}_i$ are estimated using a SLR and the covariance matrix $\boldsymbol{\Sigma}_i$ relative to the retrieved linear fit. As the range of wind speeds covered was 0 - 21 m/s, we end up with 21 wind speed bins. The wind directional dependence was removed due to the limited amount of diverse wind directional

https://doi.org/10.5194/egusphere-2026-4775
Preprint. Discussion started: 21 August 2026

data, and since findings in (Isoguchi and Shimada, 2009; Isoguchi et al., 2019) indicate that both the HH- and the HV-channel backscatter at L-band have minor wind directional dependencies.

3.1.3 Incorporating wind speed into the IA-aware Bayesian classifier

In order to account for the wind-driven variability of OW backscatter, we treat OW as a wind-dependent class during the classification process. Using wind data from the CARRA model, each pixel in a SAR image is mapped to a wind speed bin, which is then used to select the appropriate OW class parameters from the NDBC buoy - SAR data. The classification of a given pixel into either SI or OW is then a three-class problem; LI, DI, or OW_u, where OW_u is OW at wind speed u. For producing the final ice/water map, LI and DI are merged into SI. The full workflow is visualized in Figure 4.

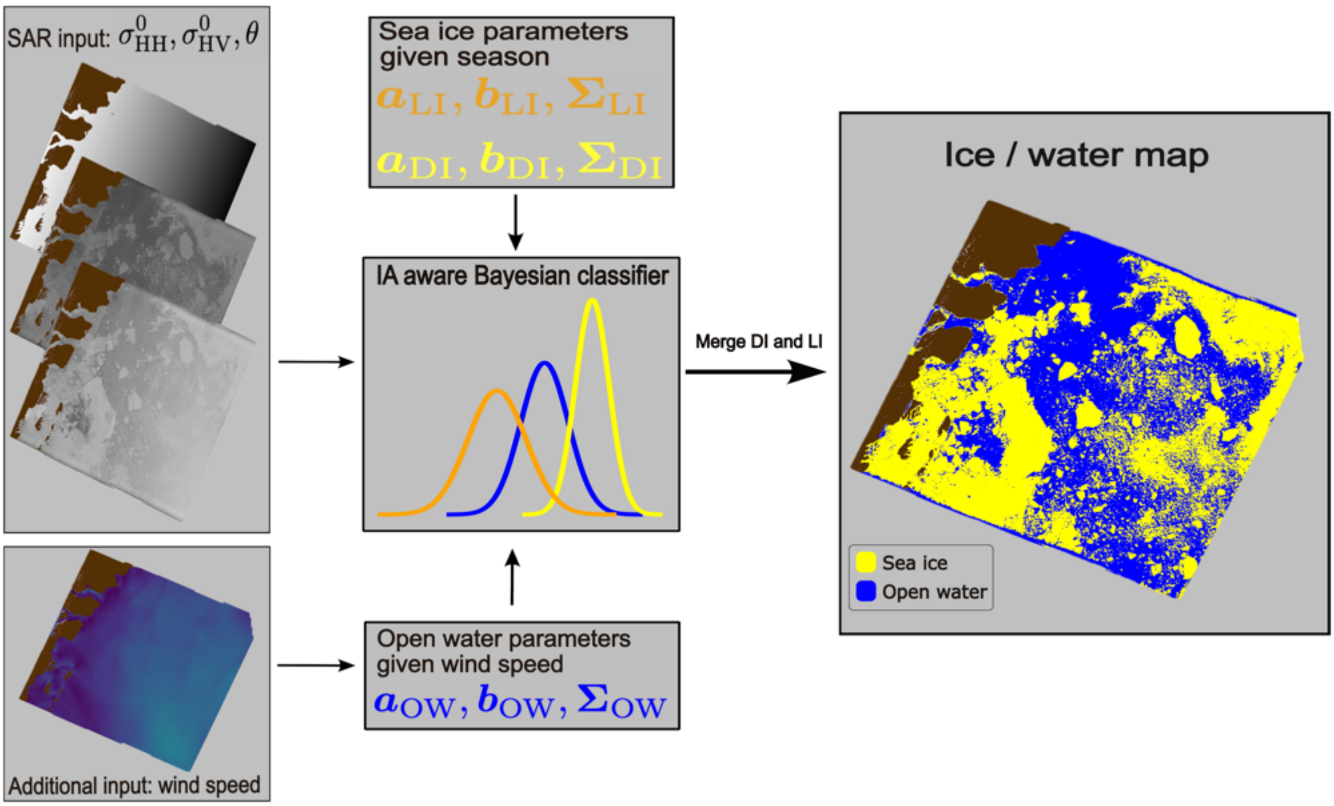

Figure 4. Visualization of the ice/water separation algorithm. External wind speed is used for the selection of the OW class parameters, while LI and DI class parameters are selected for the manually identified season. HH and HV intensity as well as IA are then used to compute the probability of a new pixel and assign it to the class with the highest probability.

By using external wind information to select just one appropriate OW class, we avoid multiple simultaneous OW classes for each wind speed, which could bias the classifier towards the narrower PDF of each OW sub-class. To demonstrate the improved accuracy achieved with this approach, we compare our method to a classifier with 21 simultaneous OW_u classes (one for each

https://doi.org/10.5194/egusphere-2026-4775
Preprint. Discussion started: 21 August 2026

wind speed bin) as well as the two ice types, where no external wind information included. Prior to computing performance metrics, the 21 OW_u classes are aggregated to one final OW class. This will be referred to as the "simultaneous-classifier".

From the ice/water map, we estimate SIC within spatial windows of size 6.25×6.25 km, to match the pixel spacing of the PMW SIC product. SIC is estimated as follows:

$$\mathrm{SIC} = \frac{\text{Number of SI pixels}}{\text{Number of valid pixels}} \times 100 \tag{4}$$

where valid pixels are pixels that do not contain land or empty pixels from the slanted boundary of the geo-referenced SAR imagery.

3.2 Evaluation of results

This subsection gives a description of the metrics we use to evaluate our results: 1) the Jeffries-Matusita (JM) distance for assessing the general class separability directly from $\boldsymbol{a}$, $\boldsymbol{b}$, and $\boldsymbol{\Sigma}$; 2) the Matthews Correlation Coefficient (MCC) and per-class accuracy (CA) for evaluating the classification results; and 3) the root mean squared distance (RMSD) to evaluate the difference between the SAR and PMW SIC estimates.

3.2.1 JM distance

We use the JM distance to assess the separability of OW and SI as a function of wind speed and IA. The JM distance is computed separately for OW–LI and OW–DI across all seasonal stages to quantify the expected performance of the classifier under specific wind and IA conditions. As a bounded measure of class separability in a two-class problem, the JM distance is defined as

$$\mathrm{JM} = 2\left(1 - e^{-D_B}\right) \tag{5}$$

where D_B is the Bhattacharyya distance (Bhattacharyya, 1946). For two multivariate Gaussian distributions, p_1 and p_2, Bhattacharyya distance is defined as

$$D_B(p_1, p_2) = \frac{1}{8}\left(\boldsymbol{\mu}_1 - \boldsymbol{\mu}_2\right)^T \boldsymbol{\Sigma}^{-1}\left(\boldsymbol{\mu}_1 - \boldsymbol{\mu}_2\right) + \frac{1}{2}\ln\left(\frac{\det\left(\frac{\boldsymbol{\Sigma}_1 + \boldsymbol{\Sigma}_2}{2}\right)}{\sqrt{\det \boldsymbol{\Sigma}_1 \det \boldsymbol{\Sigma}_2}}\right) \tag{6}$$

Unlike the Bhattacharyya distance, which ranges from 0 - ∞, the JM distance offers a standardized range of 0 - 2, where 0 indicates completely overlapping distributions and 2 indicates perfect separability. This fixed range makes the JM distance more easily interpretable (Dabboor et al., 2014). In Figure 6, the purple/pink regions correspond to low separability, while orange/yellow indicates a high separability.

https://doi.org/10.5194/egusphere-2026-4775
Preprint. Discussion started: 21 August 2026

3.2.2 Performance metrics

As the number of validation ROIs and pixels differs for SI and OW, we use the MCC to evaluate the classification results (Matthews, 1975). The MCC is designed to account for imbalanced classes, and is given as

$$\mathrm{MCC} = \frac{TP \times TN - FP \times FN}{\sqrt{(TP+FP)(TP+FN)(TN+FP)(TN+FN)}} \tag{7}$$

where TP, TN, FP and FN are the number of true positives, true negatives, false positives and false negatives respectively. The MCC is bound in the range (-1, 1), with 1 indicating a perfect prediction, 0 indicating a prediction no better than a random guess, and -1 indicating an inverse prediction.

Additionally, we evaluate the CAs, as these are easily interpretable. In this two-class problem, where we treat OW as positive and SI as negative, the CAs are given as $\mathrm{CA}_{OW} = \frac{TP}{TP+FN}$ and $\mathrm{CA}_{SI} = \frac{TN}{TN+FP}$.

3.2.3 Comparison to PMW SIC

We use the RMSD to qualitatively evaluate the difference between the SIC estimates from L-band SAR and PMW. The RMSD is bound in the range $\pm 100\%$, and is given as

$$\mathrm{RMSD} = \sqrt{\frac{\sum_{i=0}^{M}\left(\mathrm{SIC}_{i,\mathrm{SAR}} - \mathrm{SIC}_{i,\mathrm{PMW}}\right)^2}{M}} \tag{8}$$

where M is the total number of samples (i.e. pixels). The comparison to the PMW SIC dataset is not treated as an evaluation of the SAR-derived SIC, but a comparison to an existing and widely used operational product.

4 Results

This section details the main findings of the study. Section 4.1 examines the general IA dependencies, i.e. the class parameters, for OW, LI, and DI. Section 4.2 evaluates the separability of OW and both ice types using the JM distance as a metric. Finally, Section 4.3 presents the overall classification performance (MCC and CA) and SIC estimates.

4.1 Incidence angle dependencies

4.1.1 Incidence angle dependencies of ice types

The slopes, mean backscatter values evaluated at IA = 30°, and corresponding statistics for LI and DI are summarized in Tables 3 and 4 respectively. During winter, a steeper slope is observed for LI than for DI across both polarizations. This difference becomes less pronounced during melt onset, where the HV-channel slopes are equal and the HH-channel slope for LI is only slightly steeper than that of DI. During the ponding stage, the pattern reverses from winter, with steeper slopes observed for DI than LI at both polarizations. However, the standard errors (SEs) for the slope estimates are large, particularly for LI at HH. The slopes for the two ice types become similar during drainage. Notably, low R^2 scores are obtained for both LI and DI across all seasons, except during drainage. Finally, it is worth noting that the sample size for DI is consistently larger than for LI across all seasons, with the difference being most pronounced during winter and melt onset.

Overall, the mean backscatter of DI is consistently higher than that of LI across all seasons at both polarizations, though the difference is less pronounced during the melt seasons. Both ice types exhibit an increase in mean backscatter during the melting seasons compared to the winter season. This is accompanied by a corresponding decrease in standard deviation (SD), except for LI at HV during melt onset.

Table 3. Mean value and slope, with corresponding uncertainty measures, R^2 values and number of samples (n), for LI for different seasons.

Season	Polarization	$\overline{\sigma}^0_{\theta=30^\circ} \pm 1$ SD	Slope $\pm$ 1 SE	R^2	n
Winter	HH	-21.01 $\pm$ 2.38	-0.26 $\pm$ 0.04	0.29	97
	HV	-32.96 $\pm$ 1.52	-0.07 $\pm$ 0.03	0.07	
Melt onset	HH	-14.12 $\pm$ 1.50	-0.27 $\pm$ 0.04	0.34	81
	HV	-26.45 $\pm$ 1.54	-0.10 $\pm$ 0.04	0.07	
Ponding	HH	-16.95 $\pm$ 1.58	-0.18 $\pm$ 0.07	0.14	49
	HV	-27.68 $\pm$ 1.34	-0.06 $\pm$ 0.05	0.03	
Drainage	HH	-14.67 $\pm$ 1.32	-0.30 $\pm$ 0.02	0.85	72
	HV	-25.62 $\pm$ 1.33	-0.17 $\pm$ 0.02	0.59	

4.1.2 Influence of wind speed on the incidence angle dependency of L-band open water backscatter

Figure 5 presents the derived OW slope estimates (Figure 5 (a-b)) and mean backscatter intensities evaluated at IA = 30° (Figure 5 (c-d)) for each wind speed bin. The corresponding R^2-scores, sample sizes, SEs for the slope, and SDs for the mean backscatter are also provided.

The HH-channel slopes are consistently steep (approximately -0.6 dB/1°) with high R^2 values for u in the range 4 - 15 m/s. At $u \leq 4$ m/s the slope magnitude increases rapidly from around -0.1 to -0.5 dB/1°, albeit with low accompanying R^2 scores. The slope magnitude is highly variable for $u > 15$ m/s, with large corresponding SEs. While the R^2 scores remain high for

https://doi.org/10.5194/egusphere-2026-4775
Preprint. Discussion started: 21 August 2026

Table 4. Mean value and slope, with corresponding uncertainty measures, R^2 values and number of samples (n), for DI for different seasons.

Season	Polarization	$\overline{\sigma}^0_{\theta=30°} \pm 1$ SD	Slope $\pm$ 1 SE	R^2	n
Winter	HH	-16.97 ± 2.49	-0.17 ± 0.02	0.15	585
	HV	-29.73 ± 2.66	0.01 ± 0.02	0.00	
Melt onset	HH	-12.58 ± 1.39	-0.22 ± 0.02	0.40	239
	HV	-24.22 ± 1.55	-0.10 ± 0.02	0.09	
Ponding	HH	-14.18 ± 1.67	-0.23 ± 0.04	0.29	68
	HV	-24.60 ± 1.77	-0.13 ± 0.05	0.10	
Drainage	HH	-12.59 ± 0.97	-0.30 ± 0.01	0.88	121
	HV	-22.90 ± 1.07	-0.21 ± 0.01	0.75	

these high-wind cases, the small sample sizes limit their statistical reliability. Parallel to these slope variations, the mean backscatter increases logarithmically with wind speed, exhibiting a rapid rise at $u \leq 4$ m/s before tapering off into a slower, near-asymptotic increase at higher wind speeds. The SDs also drop sharply, from ~ 5 dB in the $u \leq 4$ m/s range to $\sim 1-2$ dB at higher wind speeds.

For the HV-channel, the slope estimates are far less consistent than for the HH-channel, with low R^2 scores throughout. The slopes decrease gradually from $\sim$ 0.1 to -0.2 dB/1° in the low-wind range ($u \leq 4$ m/s), while for the higher wind speeds they fluctuate around -0.2 dB / 1° with no apparent trend. While the mean backscatter increases with wind speed, rising from roughly -35 ± 5 dB to -23 ± 2 dB, the mean intensities remain below or close to the NESZ for wind speeds up to 12 m/s. For the higher wind speeds, the small sample sizes limit the reliability of the estimates. Consistently high SDs ($\sim 2-5$ dB) are subsequently observed across all wind speeds.

4.2 Separability of sea ice and open water as a function of wind speed and incidence angle

The JM distance is used to evaluate the separability of OW against each ice type, across the full range of IAs and wind speeds. This evaluation is conducted per season, with the results illustrated in Figure 6, where the purple/pink regions correspond to low separability, while orange/yellow indicates a high separability.

A diagonal band of reduced separability (JM < 1), exhibiting an inverse relationship between IA and wind speed, is present for both ice types across all seasons, though it is most pronounced during winter. During the winter season, low separability extends across the entire IA range for the OW–LI combination for at $u < 3$ m/s. Throughout the melt seasons, OW–LI sep-

https://doi.org/10.5194/egusphere-2026-4775
Preprint. Discussion started: 21 August 2026

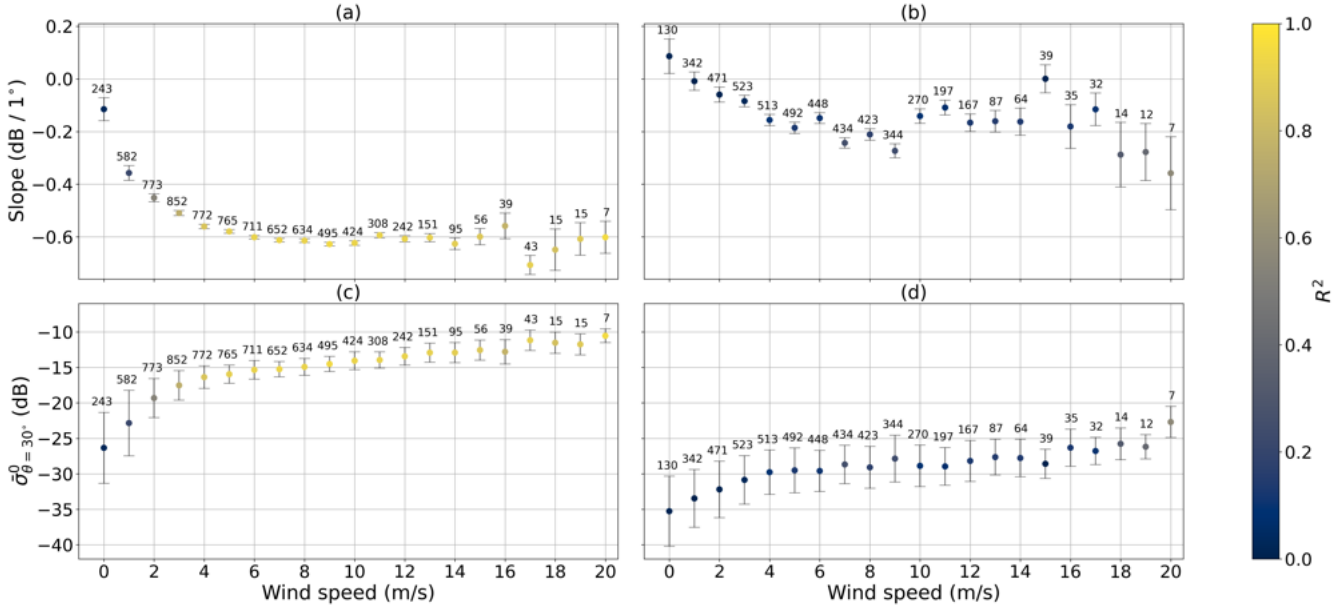

Figure 5. Backscatter slopes as a function of IA for the HH- and HV-channels (a-b), together with mean backscatter evaluated at IA=30° (c-d) per wind speed bin. The number of samples used to calculate the slope and mean values are included as annotations. All estimates are color-coded by the R^2 value of the SLR. The error bars show the SE and SD for the slopes and mean values respectively.

arability remains consistently lower than that of OW–DI, though the regions of low separability for both ice types are less pronounced compared to winter.

4.3 Evaluation of sea ice and open water classification

The MCC-scores and CAs for both the wind-informed, and simultaneous classifier are presented in Tables 5 and 6, respectively. The wind-informed classifier consistently outperforms the simultaneous classifier across all seasons, with the simultaneous classifier being biased towards OW as expected (see Section 3.1.3). As the wind-informed classifier is the main focus of the study, and we demonstrate that it outperforms the more simplistic simultaneous classifier, the rest of the results section will be dedicated to the wind-informed classifier.

Consistently high MCC scores are achieved (MCC > 0.800) for all three stages of the melt season, with the highest accuracies during drainage. During the melt onset and ponding stages, the CA values for SI are somewhat lower than for OW, indicating a slight bias towards OW. This bias is not apparent during drainage, where the CAs are similarly high. A significantly lower MCC score of 0.506 is achieved for the winter season. From the CA it is evident that the classifier struggles to correctly identify OW during this season, significantly biasing it towards SI.

https://doi.org/10.5194/egusphere-2026-4775
Preprint. Discussion started: 21 August 2026

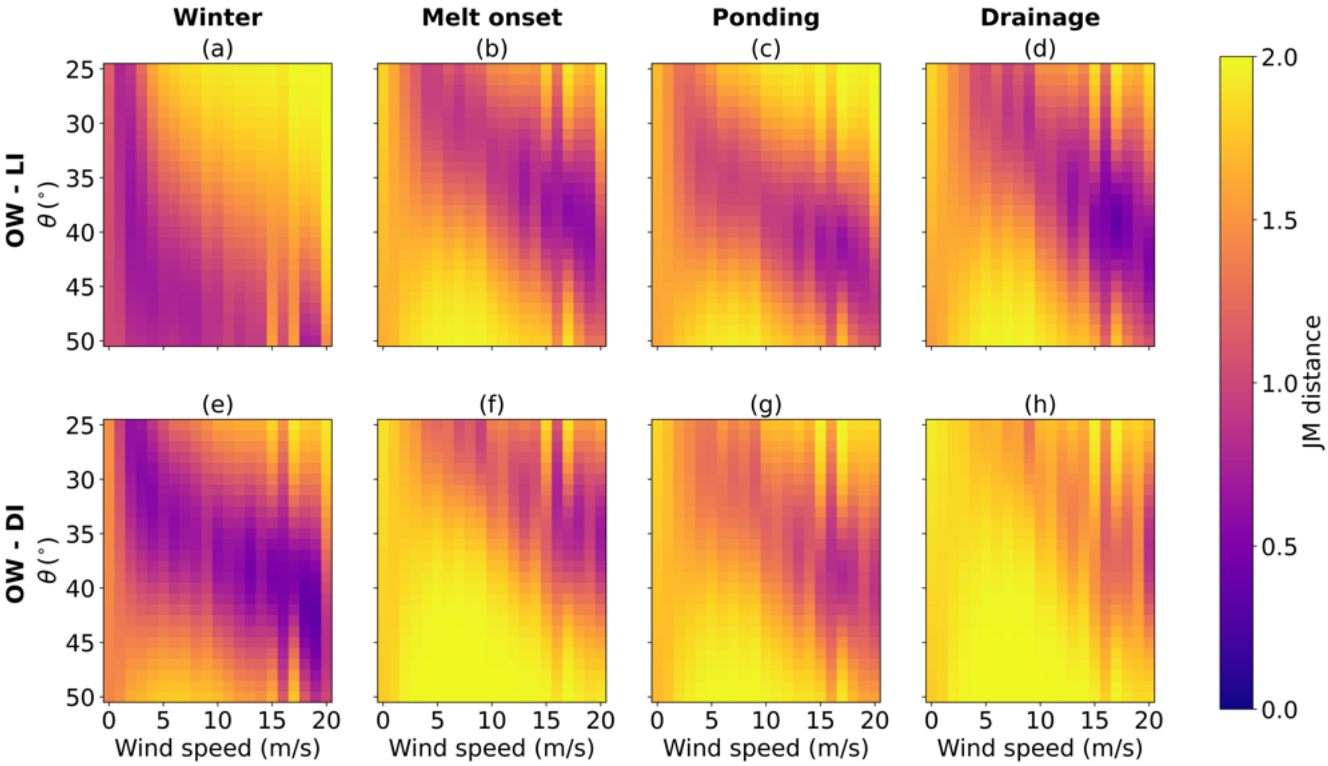

Figure 6. JM distance as a function of IA (y-axis) and wind speed (x-axis) per season for OW-LI (top row) and OW-DI (bottom row). Blue/purple regions indicate combinations of IA and wind speed where the separability between OW and an ice type is low, while orange/yellow regions indicates high separability.

Table 5. CAs for SI and OW and MCC scores, for all seasons and per season for the wind-informed classifier.

	Overall	Winter	Melt onset	Ponding	Drainage
CA_{SI}	0.863	0.888	0.777	0.834	0.949
CA_{OW}	0.970	0.590	0.995	0.997	0.989
MCC	0.851	0.506	0.842	0.883	0.934

Table 6. CAs for SI and OW and MCC scores, for all seasons and per season for the simultaneous classifier.

	Overall	Winter	Melt onset	Ponding	Drainage
CA_{SI}	0.606	0.437	0.576	0.603	0.847
CA_{OW}	0.987	0.819	0.997	1.000	0.994
MCC	0.684	0.250	0.708	0.727	0.832

https://doi.org/10.5194/egusphere-2026-4775
Preprint. Discussion started: 21 August 2026

4.3.1 Comparison between SAR and PMW SIC

In Figures 7 - 10, we present selected example images from each seasonal stage. Each figure contains the classification results, L-band SAR imagery (HH- and HV-channel), overlapping optical imagery, PMW- and SAR-derived SIC estimates, the difference between the SAR and PMW SIC estimates (Δ SIC) and the CARRA wind speed map.

Figure 7 shows an example from the ponding season. In this example, the wind-informed classifier successfully manages to separate SI and OW in the presence of a varying wind field (Figure 7 (f)), which manifests as varying backscatter intensity over OW, particularly in the HH-channel (Figure 7 (e)). The wind-informed classifier successfully detects small ice floes, which can not be detected from PMW due to the coarse spatial resolution (Figure 7 (c)). Despite an overall high classification accuracy in this example, a small region of misclassification occurs in the top left corner of the scene, where a portion of SI is mistaken for OW. Overall, SIC is underestimated in the PMW imagery in this example, resulting in an RMSD of 15.5%.

In Figure 8, an example from the drainage season is shown. Accurate separation of SI and OW is achieved in this example as well, with smaller features like floes and brash ice correctly identified from the SAR imagery. A strong gradient in wind speed (Figure 8 (h)), and subsequently in HH-channel backscatter intensity (Figure 8 (e)), from right to left in the scene is observed. While the right side of the optical imagery (Figure 8 (g)) is obscured by clouds, visual inspection of the HV-channel image (Figure 8 (f)) indicates that the varying wind field does not impact the classification accuracy. Despite a generally similar visual appearance of the SAR and PM SIC images in Figures 8 (b) and (c), the difference image (Figure 8 (d)) reveals some areas of large disagreement between the two products, partly because a lot of brash ice is incorrectly interpreted as OW in the PMW imagery (the middle section of the scene). Of the shown examples, this had the largest discrepancy between SAR and PMW SIC, with RMSD = 28.0%.

An example from melt onset is shown in Figure 9. As in the last two examples, the classifier manages to detect smaller features like small ice floes, brash ice, and leads (9 (a)), which are not captured in the PMW SIC estimate (Figure 9 (c)). There is also a clear boundary between regions of high and low wind speeds in the CARRA data (Figure 9 (h)), which manifests as a region of dark OW backscatter in the SAR imagery. This does not appear to make a noticeable impact on the classification results (Figure 9 (a)), indicating that the wind-informed classifier successfully accounts for the wind speed variations in this case. However, a large region consisting of larger floes and brash ice is misclassified as mostly OW in the SAR classification map (the magenta square). This region is in the near-range of the SAR image, with corresponding wind speeds in the 5-10 m/s range. Separability is low for both OW-LI and OW-DI for this combination of IA and wind speed during melt onset (Figure 6 (b) and (f)), particularly for LI. From visual inspection of the optical imagery (Figure 9 (g)) as well as the source SAR imagery (Figure 9 (e-f)), it is evident that the classifier produces an error in this case, which is correctly identified as high SIC in the PMW imagery. Overall, there are large discrepancies between the SAR and PMW SIC estimates (Figure 9 (d)), with an RMSD of 19.8%.

Lastly, an example from the winter season is shown in Figure 10. This scene consists mainly of SI, with some leads being present. Much of the scene is classified correctly, though a large portion of SI is misclassified as OW (the magenta square in Figure 10 (a)). While the cause of this is not entirely clear, it may reflect a limitation of the two SI classes that we defined for

https://doi.org/10.5194/egusphere-2026-4775
Preprint. Discussion started: 21 August 2026

this study, leading to some SI not fitting well into either of their respective PDFs. Scalloping effects are also present in the right portion of the ice/water map, manifesting as striping in the range direction. There is an overall large discrepancy between the SAR and PMW SIC estimates (Figure 10 (d)), with an RMSD of 20.6%.

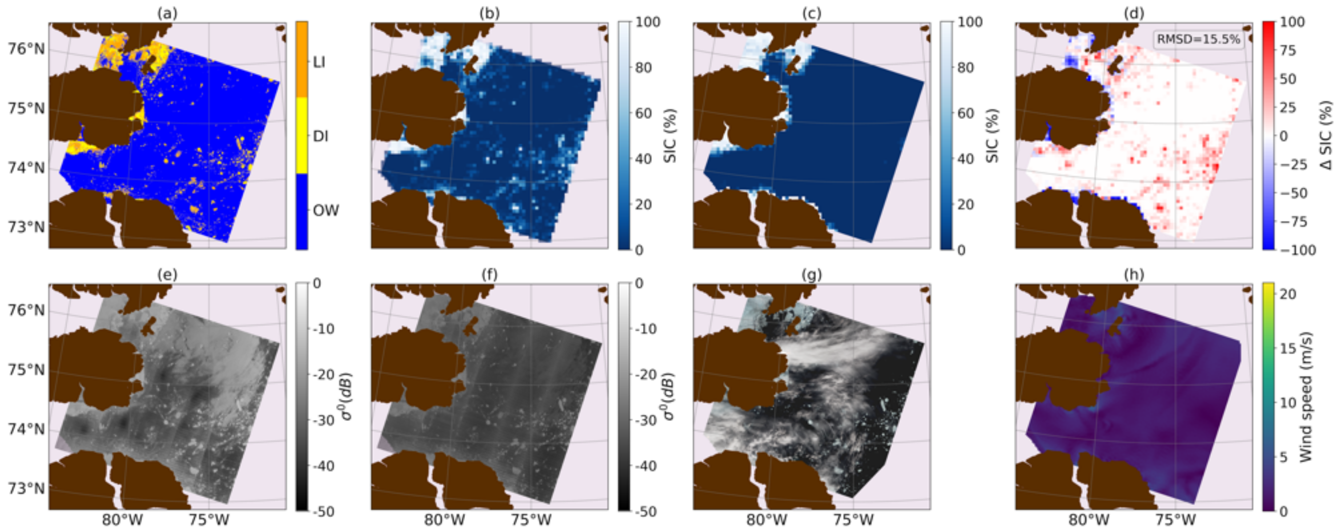

Figure 7. Classified L-band SAR image (a), SIC from L-band SAR (b) and PMW (c), SIC difference between SAR and PMW (d), HH- and HV-channel SAR images (e-f), overlapping S3 RGB image (g) and corresponding CARRA wind speeds (h). In (d), red indicates a higher SIC in the SAR product while blue indicates a higher SIC in the PMW product. Date: 09-07-2019. Region: CAA. Season: ponding

5 Discussion

5.1 Incidence angle dependencies

Ice-type specific slopes of backscatter intensity with IA for L-band SAR were reported in (Mahmud et al., 2018) for the HH-channel in winter, and for both the HH- and HV-channels during winter, melt onset and advanced melt (ponding and drainage merged) in (Karlsen et al., 2024). Our IA slopes (Tables 3 and 4) differ somewhat from these values. We suggest two possible reasons for the differences: (1) the different methods used to estimate the IA dependency and (2) the inclusion of several test sites in our SI ROIs. The former was necessary as we wanted to capture a broad range of SI conditions over both landfast and drifting ice, meaning that subsequent SAR scenes over the same region with different viewing geometries were not available. We subsequently could not use the differencing method described in e.g. (Mäkynen and Karvonen, 2017; Geldsetzer and Howell, 2023; Karlsen et al., 2024) to estimate the SI IA dependencies. While the differencing method can offer superior accuracy when applied to a SAR time-series — particularly when the distribution of IAs is non-homogeneous — estimating the IA dependency directly via SLR was the only viable option in our case. Additionally, the inclusion of several Arctic test sites (Figure 1) meant that we could retrieve more generalized model parameters, which are hence suited for pan-

https://doi.org/10.5194/egusphere-2026-4775
Preprint. Discussion started: 21 August 2026

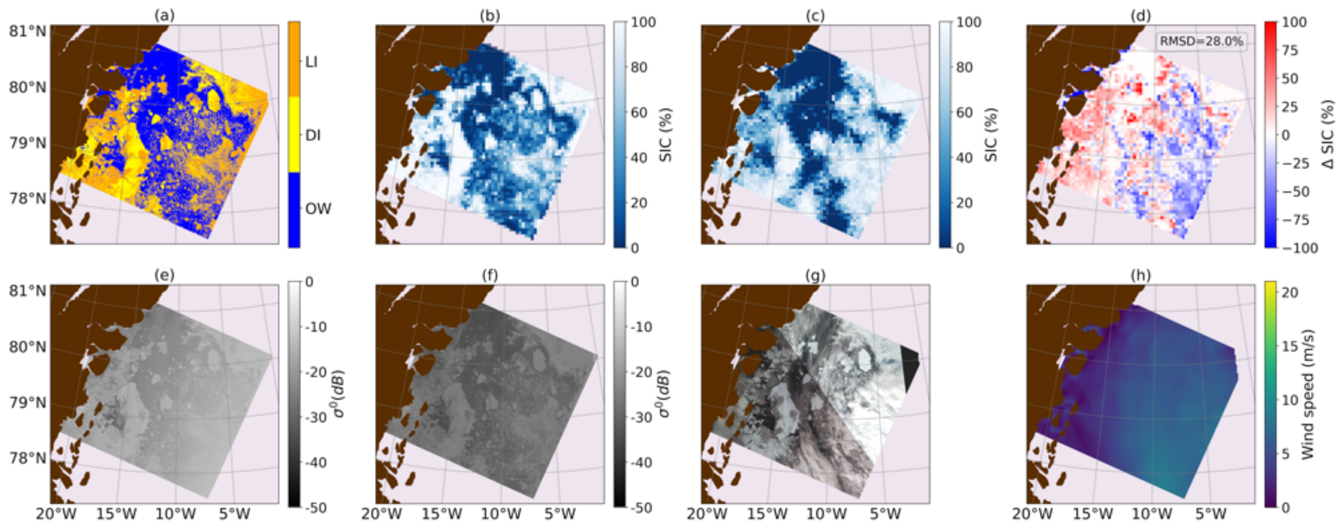

Figure 8. Classified L-band SAR image (a), SIC from L-band SAR (b) and PMW (c), SIC difference between SAR and PMW (d), HH- and HV-channel SAR images (e-f), overlapping S3 RGB image (g) and corresponding CARRA wind speeds (h). In (d), red indicates a higher SIC in the SAR product while blue indicates a higher SIC in the PMW product. Date: 04-08-2019. Region: FS. Season: drainage

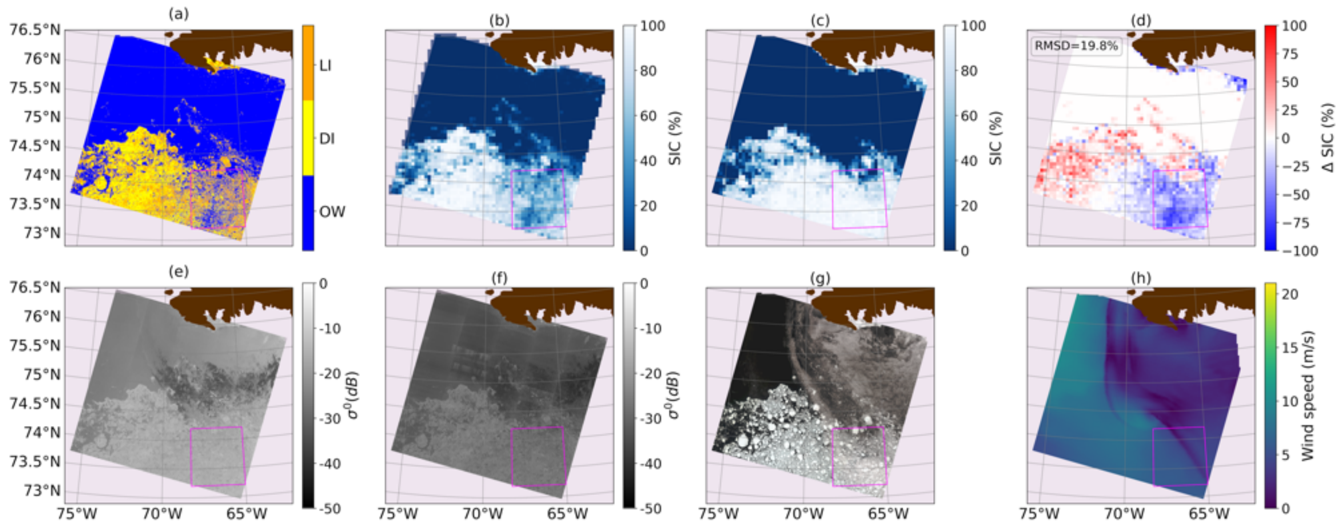

Figure 9. Classified L-band SAR image (a), SIC from L-band SAR (b) and PMW (c), SIC difference between SAR and PMW (d), HH- and HV-channel SAR images (e-f), overlapping S3 RGB image (g) and corresponding CARRA wind speeds (h). In (d), red indicates a higher SIC in the SAR product while blue indicates a higher SIC in the PMW product. The magenta square highlights a large region where SI is misclassified as OW. Date: 31-05-2019. Region: CAA. Season: melt onset

https://doi.org/10.5194/egusphere-2026-4775
Preprint. Discussion started: 21 August 2026

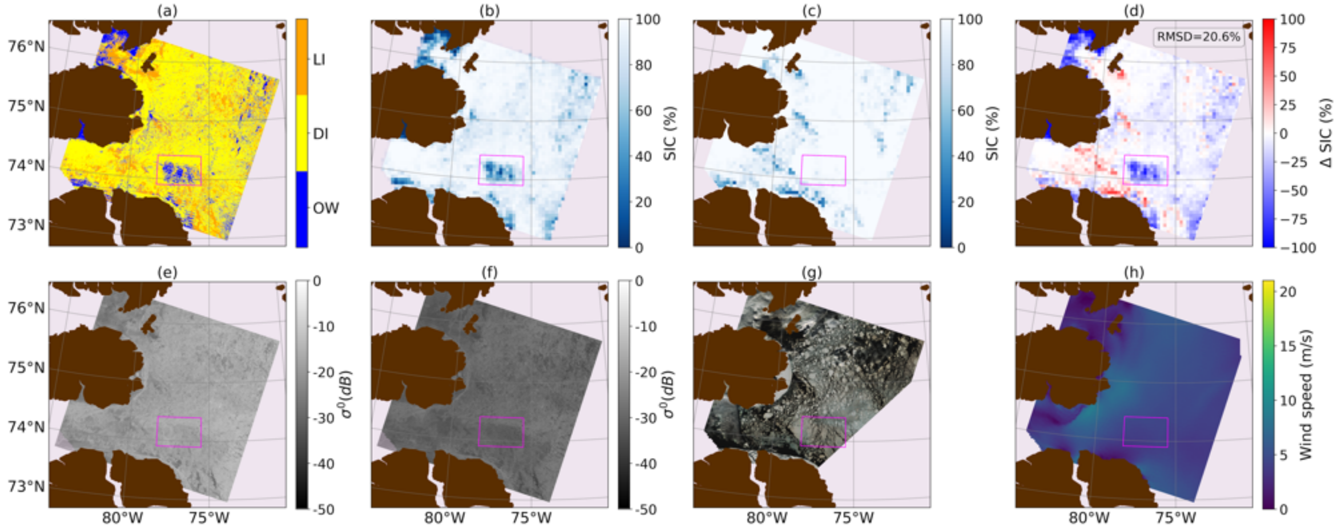

Figure 10. Classified L-band SAR image (a), SIC from L-band SAR (b) and PMW (c), SIC difference between SAR and PMW (d), HH- and HV-channel SAR images (e-f), overlapping S3 RGB image (g) and corresponding CARRA wind speeds (h). In (d), red indicates a higher SIC in the SAR product while blue indicates a higher SIC in the PMW product. The magenta square highlights a large region where SI is misclassified as OW. Date: 30-04-2019. Region: CAA. Season: winter

Arctic coverage without the need to adjust ice class parameters based on regional differences. At the same time, this means that a broader distribution of ice conditions must fit within the description of the two ice types, possibly making the more generalized classifier less accurate for specific local SI conditions.

Our OW IA slopes for HH are slightly shallower (~ -0.6 dB / $1°$ for $u \geq 4$ m/s) than those observed by (Isoguchi et al., 2019), who estimated slopes around -0.7 dB / $1°$ for the wind speed range 0 - 15 m/s. Their slope magnitudes also increased slightly with wind speed, which we did not observe (Figure 5 (a)). For the HV-channel, they found that the slope magnitude decreased from around -0.4 dB / $1°$ at $u = 0$ m/s to roughly -0.1 dB / $1°$ for $u = 15$ m/s. Here we found no consistent pattern between our slope estimates and wind speed in the HV-channel (Figure 5 (b)). We assume that part of the reason for this discrepancy is noise related, as noise contamination is most prominent in low-backscatter areas, such as OW at low wind speeds for HH and all wind speeds included in this study for HV (Figure 3), which are the conditions where we observe the most pronounced differences between our estimates and the ones presented in (Isoguchi et al., 2019). We make use of ALOS-2 imagery in L2.2 format, which is provided without noise removal applied, or the information to remove system noise. Hence, significant scalloping remains in the imagery. To mitigate the scalloping, we use a Gaussian notch filter (see Section 2.2.1). This noise filtering, which was not done by Isoguchi et al. could be a contributing factor to the discrepancies observed.

For some of our slope and intercept estimates, the sample sizes are small. This is the case for DI during ponding, for LI across all seasonal stages, and for OW at higher wind speeds ($n_{\mathrm{HH}} < 100$ for $u \geq 14$m/s; $n_{\mathrm{HV}} < 100$ for $u \geq 13$m/s). For OW, increased variability in the slope magnitudes and larger SEs are observed for these conditions, which is likely a result of the

https://doi.org/10.5194/egusphere-2026-4775
Preprint. Discussion started: 21 August 2026

smaller sample sizes. High winds are known to be less prevalent (Isoguchi and Shimada, 2009), which makes these inaccuracies less critical in the context of ice/water separation. For DI, slightly larger SEs are observed during ponding compared to the remaining seasons, while no consistent pattern for the R^2-scores are observed. The presence of larger SE for the melt season stages was in (Casey et al., 2016) attributed to changes in dominant scattering mechanisms. The LI SEs are generally higher than for DI, which we attribute to both the small sample sizes and overall weaker backscatter intensity of LI compared to DI. While small sample sizes could affect the accuracies of the estimated IA slopes, statistical classifiers such as the one used here generally require much less data compared to more advanced machine learning algorithms such as CNNs (Wu et al., 2026).

5.2 Separability of sea ice and open water as a function of wind speed and incidence angle

We assessed the separability of OW against both ice types as a function of wind speed and IA, using the JM as a measure of separability. During the melt seasons (Figure 6 (f-h)), the regions of low separability between DI and OW are significantly smaller compared to winter (Figure 6 (e)), allowing the classifier to resolve most wind speed and IA combinations. The remaining zones of low separability are concentrated at wind speeds ≥ 10 m/s, which are less prevalent (Isoguchi and Shimada, 2009). Conversely, we observe lower separability between OW and LI, particularly during the winter season (Figure 6 (a)), where low separability was observed across the entire IA range for $u \leq 3$ m/s. Better results were achieved during the melting seasons (Figure 6 (b-d)), though regions of low separability persisted. The improved results during the melt season is in line with observations in (Casey et al., 2016), where they found smaller backscatter variation between different ice types during advanced melt than during the winter and early melt period regardless of incidence angle. In addition to improved SIC estimates, these results also demonstrate that our method is well suited for distinguishing DI from OW specifically, which is a major operational advantage given that DI is both the most prevalent ice type and the primary hazard vessels must avoid (Lohse et al., 2024). Our classifier is also expected to perform well under the conditions most critical for Arctic shipping: summer melting periods and calm wind conditions.

5.3 Evaluation of sea ice and open water classification

From Tables 5 and 6, it is evident that the wind-informed classifier outperforms the simultaneous classifier across all seasonal stages. This demonstrates the usefulness of including a wind speed dependent OW class, instead of using several OW classes for different wind conditions simultaneously. Similarly, we would expect a classifier with only one broad OW class covering all wind speeds to perform poorly, as the resulting PDF would be broad and subsequently give low OW probabilities.

Overall, our comparison between the SAR and PMW derived SIC products indicate that L-band SAR outperforms PMW during the summer months (Figures 7 - 9), achieving high classification accuracy whilst maintaining a fine spatial resolution. This is in line with what was found in (Karvonen et al., 2020). During the melt seasons, we achieve accurate and reliable results without incorporating textural information, by accounting for the variability of OW backscatter through the use of external wind information. This is beneficial, as texture features increases computational costs and requires the selection of appropriate parameters (Lohse et al., 2021). Furthermore, traditional texture features require a choice for the window size. For C-band, Lohse et al. showed that large texture windows of 51x51 pixels are needed for reliable ice/water separation (Lohse

https://doi.org/10.5194/egusphere-2026-4775
Preprint. Discussion started: 21 August 2026

et al., 2021). Besides the computational cost, such large texture windows effectively reduce the spatial resolution of the final ice/water map and resulting SIC estimates. While overall good performance was achieved during the melt onset season without textural information, some errors occurred. For example, the magenta box in Figure 9 highlights a region in the SAR image where SI is misclassified as OW. This occurs in the near-range, where separability between both ice types and OW is low in the 5-10 m/s wind speed range during melt onset, which are the wind speeds corresponding to this area (Figure 9 (h)). This suggests that incorporating textural information could be beneficial for reliable separation of SI and OW during melt onset as well.

However, during winter conditions, reliable separation of SI and OW was not achieved based on backscatter alone, even with external wind information. This is in line with the findings in (Karvonen et al., 2020) where discrimination between SI and OW based on L-band backscatter alone was unreliable, though inclusion of texture parameters improved ice/water separation in winter conditions. Based on the results in Figure 6 we observe large regions of overlapping backscatter for both OW-LI and OW-DI during the winter season. Incorporating textural information into our wind-informed classifier could therefore be an option to improve performance during the winter season. Alternatively, contextual information could be incorporated through the use of CNNs, as has been shown for C-band SAR in multiple studies, e.g. (Radhakrishnan et al., 2021; Wang et al., 2023; Wulf et al., 2024; Rusin et al., 2025; Wulf et al., 2026; Rusin et al., 2026). While these methods have been shown to produce accurate results, large amounts of labeled training data are needed for accurate training of the network. This is currently a limitation for L-band SAR. However, with several recently launched and upcoming missions (ALOS-4, NISAR, ROSE-L), L-band SAR imagery will become more abundant in the near future.

5.4 Current limitations and future work

For accurate and reliable classification of SI and OW in the winter season, as well as to improve the separability of LI and OW in general, the inclusion of textural information could be incorporated. The inclusion of wind direction could also potentially improve performance, though regions of overlapping backscatter between OW and SI will anyways be present. A significantly denser reference dataset would also be needed to evaluate IA dependency at all combinations of wind speed and direction, which at the present was not available to us. Yet another option would be to implement the method presented in (Komarov and Buehner, 2017) for L-band SAR, though this requires an accurate L-band GMF for both the HH- and HV-channels, which at the present is not available.

A major limitation of our method is that seasonality must currently be assigned manually to the SAR data. Developing a robust approach for automatically determining the seasonal stage of each image is therefore essential for fully automating the method. However, unambiguously assigning seasonal stages based on auxiliary information — such as air temperature, PMW, or optical data — is challenging, particularly during the melt season, when SI conditions can change rapidly. Incorrectly assigning a seasonal stage to a scene would result in inappropriate parameters being used for LI and DI. Because backscatter signatures —and, consequently, class parameters—can vary substantially across seasons for a given ice type (Tables 3, 4), selecting the wrong class parameters could severely impact the accuracy of the classifier. Furthermore, the misclassification highlighted by the magenta square in Figure 10 indicates that the addition of further SI types may improve ice/water separation

https://doi.org/10.5194/egusphere-2026-4775
Preprint. Discussion started: 21 August 2026

in some cases. In this example, a SI area with weak HV and strong HH backscatter is misclassified as OW. Based on our definition and ROI selection for LI and DI, this particular ice type likely does not fit well into either of the class descriptions. The weak HV backscatter suggests little or no presence of large-scale surface deformation features, while the simultaneously strong HH backscatter indicates a significant degree of small-scale surface roughness, resulting in more diffuse scattering leading to the stronger co-polarized signal. Explicitly training an additional SI class for rough (small-scale) level (large-scale) ice might help to avoid such misclassification in the future. However, it should be kept in mind that the introduction of additional SI types may result in a bias of the binary ice/water maps towards SI, similarly to the inclusion of all separate wind speed OW classes at the same time in the simultaneous classifier led to a bias towards OW. Adding region-specific ice-types also reduces the generality of the model.

Finally, the methodology presented in this study is demonstrated on L-band SAR imagery, specifically for the purpose of separating SI from OW under varying wind conditions. However, our method would also be suited for SAR systems operating at other wavelengths, such as X-, C-, S- and P-band, which are the other current wavelengths used by space-borne SAR systems. Moreover, as a general framework, the concept of using external information (in this case wind speed) to decide class parameters would also be suitable to other applications where class characteristics vary with external conditions.

6 Conclusions

In this study, we improved an IA-aware Bayesian maximum likelihood ice-type classifier by incorporating external wind information to account for wind-driven variability in OW backscatter at L-band. By integrating model-derived wind speeds into the forward classification of SAR scenes, the framework conditionally selects optimal OW class parameters from a reference dataset of empirically estimated IA dependencies. Compared with a classifier that does not incorporate wind information, the proposed approach consistently yields higher classification accuracy. The wind-informed method enables accurate, high-resolution classification of SI and OW during melt conditions without relying on computationally expensive texture features. It can therefore produce high-resolution and accurate SIC estimates during a period when PMW products are known to overestimate SIC. In winter, however, low SI backscatter and system-noise limitations reduce classification reliability. These findings suggest that while integrating textural information remains a necessity for reliable ice/water separation during winter conditions, L-band backscatter intensity combined with external wind data enables accurate classification of SI and OW during the dynamic melt season. As L-band SAR observations become increasingly available through missions such as ALOS-4, NISAR, and ROSE-L, this approach offers a scalable pathway toward more accurate, high-resolution monitoring of sea ice during the melt season.

Acknowledgements. The data used for this paper have been provided by Earth Observation Research Center (EORC) of Japan Aerospace Exploration Agency (JAXA). The presented work contains primary and altered Sentinel data products (@Copernicus data).

Code availability. Code for processing and classifying ALOS-2 L2.2 imagery into sea ice or open water is available upon request.

Data availability. All data used in this work is freely and openly available; ALOS-2 L2.2 imagery from Google earth engine and gportal, Sentinel-2 and -3 from Copernicus Browser, CARRA from the Copernicus Climate Change Service, NDBC buoy data from NOAA.

Author contributions. TK prepared the manuscript with key contributions from JL, MJ, RS and APD. The scientific investigation was conducted by TK, with key contributions from JL, RS, APD and MJ. TK and RS defined the research question. TK and JL designed the study.

Competing interests. The authors declare no competing interest

https://doi.org/10.5194/egusphere-2026-4775
Preprint. Discussion started: 21 August 2026

References

Aldenhoff, W., Heuzé, C., and Eriksson, L. E.: Comparison of ice/water classification in Fram Strait from C-and L-band SAR imagery, Annals of Glaciology, 59, 112–123, 2018.

Barber, D. G., Yackel, J., and Hanesiak, J.: Sea ice, RADARSAT-1 and Arctic climate processes: A review and update, Canadian Journal of Remote Sensing, 27, 51–61, 2001.

Bhattacharyya, A.: On a measure of divergence between two multinomial populations, Sankhyā: the indian journal of statistics, pp. 401–406, 1946.

Casey, J., Howell, S., Tivy, A., and Haas, C.: Separability of sea ice types from wide Swath C- and L-band synthetic aperture radar imagery acquired during the melt season, Remote Sensing of Environment, 174, 314–328, 2016.

Center, N. D. B.: Handbook of Automated Data Quality Control Checks and Procedures, Tech. Rep. NDBC Technical Document T80-10, National Oceanic and Atmospheric Administration, https://www.ndbc.noaa.gov/publications/NDBCHandbookofAutomatedDataQualityControl2023.pdf, 2023.

Comiso, J. C. and Parkinson, C. L.: Arctic sea ice parameters from AMSR-E data using two techniques and comparisons with sea ice from SSM/I, Journal of Geophysical Research: Oceans, 113, 2008.

Dabboor, M., Howell, S., Shokr, M., and Yackel, J.: The Jeffries–Matusita distance for the case of complex Wishart distribution as a separability criterion for fully polarimetric SAR data, International journal of remote sensing, 35, 6859–6873, 2014.

Fu, L.-L. and Holt, B.: Some examples of detection of oceanic mesoscale eddies by the SEASAT synthetic-aperture radar, Journal of Geophysical Research: Oceans, 88, 1844–1852, 1983.

Geldsetzer, T. and Howell, S. E.: Incidence angle dependencies for C-band backscatter from sea ice during both the winter and melt season, IEEE Transactions on Geoscience and Remote Sensing, 61, 1–15, 2023.

Gonzalez, R. C. and Woods, R. E.: in: Digital Image Processing, chap. 5.4, Pearson Education, New York, NY, 4th edn., 2018.

Hsu, S., Meindl, E. A., and Gilhousen, D. B.: Determining the power-law wind-profile exponent under near-neutral stability conditions at sea, Journal of Applied Meteorology (1988-2005), pp. 757–765, 1994.

Isoguchi, O. and Shimada, M.: An L-band ocean geophysical model function derived from PALSAR, IEEE Transactions on Geoscience and Remote Sensing, 47, 1925–1936, 2009.

Isoguchi, O., Ishizuka, K., Tadono, T., Motohka, T., and Shimada, M.: Effect of Faraday rotation on L-band ocean normalized radar cross section and wind speed detection, IEEE Journal of Selected Topics in Applied Earth Observations and Remote Sensing, 12, 2477–2485, 2019.

Johansson, A., King, J., Doulgeris, A. P., Gerland, S., Singha, S., Spreen, G., and Busche, T.: Combined observations of A rctic sea ice with near-coincident colocated X-band, C-band, and L-band SAR satellite remote sensing and helicopter-borne measurements, Journal of Geophysical Research: Oceans, 122, 669–691, 2017.

Johansson, A. M., Brekke, C., Spreen, G., and King, J. A.: X-, C-, and L-band SAR signatures of newly formed sea ice in Arctic leads during winter and spring, Remote Sensing of Environment, 204, 162–180, 2018.

Karlsen, T., Johansson, M., Lohse, J., and Doulgeris, A. P.: Incidence angle dependency and seasonal evolution of L and C-band SAR backscatter over landfast sea ice, Annals of Glaciology, 65, e29, 2024.

Karvonen, J.: Baltic sea ice concentration estimation based on C-band dual-polarized SAR data, IEEE Transactions on Geoscience and Remote Sensing, 52, 5558–5566, 2013.

https://doi.org/10.5194/egusphere-2026-4775
Preprint. Discussion started: 21 August 2026

Karvonen, J.: A sea ice concentration estimation algorithm utilizing radiometer and SAR data, The Cryosphere, 8, 1639–1650, 2014.

Karvonen, J., Rinne, E., Sallila, H., and Mäkynen, M.: On suitability of ALOS-2/PALSAR-2 dual-polarized SAR data for Arctic sea ice parameter estimation, IEEE Transactions on Geoscience and Remote Sensing, 58, 7969–7981, 2020.

Kern, S., Lavergne, T., Notz, D., Pedersen, L. T., and Tonboe, R.: Satellite passive microwave sea-ice concentration data set inter-comparison for Arctic summer conditions, The Cryosphere, 14, 2469–2493, 2020.

Køltzow, M., Schyberg, H., Støylen, E., and Yang, X.: Value of the Copernicus Arctic Regional Reanalysis (CARRA) in representing near-surface temperature and wind speed in the north-east European Arctic, Polar Research, 41, 2022.

Komarov, A. S. and Buehner, M.: Automated detection of ice and open water from dual-polarization RADARSAT-2 images for data assimilation, IEEE Transactions on Geoscience and Remote Sensing, 55, 5755–5769, 2017.

Komarov, A. S. and Buehner, M.: Ice concentration from dual-polarization SAR images using ice and water retrievals at multiple spatial scales, IEEE Transactions on Geoscience and Remote Sensing, 59, 950–961, 2020.

Lavergne, T., Kern, S., Aaboe, S., Derby, L., Dybkjaer, G., Garric, G., Heil, P., Hendricks, S., Holfort, J., Howell, S., et al.: A new structure for the sea ice essential climate variables of the global climate observing system, Bulletin of the American Meteorological Society, 103, E1502–E1521, 2022.

Lohse, J., Doulgeris, A. P., and Dierking, W.: Mapping sea-ice types from Sentinel-1 considering the surface-type dependent effect of incidence angle, Annals of Glaciology, 61, 260–270, 2020.

Lohse, J., Doulgeris, A. P., and Dierking, W.: Incident angle dependence of Sentinel-1 texture features for sea ice classification, Remote Sensing, 13, 552, 2021.

Lohse, J., Taelman, C., Everett, A., and Hughes, N. E.: Automated Sentinel-1 sea ice type mapping and in-situ validation during the CIRFA-22 cruise, Annals of Glaciology, 65, e39, 2024.

Mahmud, M. S., Geldsetzer, T., Howell, S. E., Yackel, J. J., Nandan, V., and Scharien, R. K.: Incidence angle dependence of HH-polarized C-and L-band wintertime backscatter over Arctic sea ice, IEEE Transactions on Geoscience and Remote Sensing, 56, 6686–6698, 2018.

Mahmud, M. S., Nandan, V., Howell, S. E., Geldsetzer, T., and Yackel, J.: Seasonal evolution of L-band SAR backscatter over landfast Arctic sea ice, Remote Sensing of Environment, 251, 112 049, 2020.

Mahmud, M. S., Nandan, V., Singha, S., Howell, S. E., Geldsetzer, T., Yackel, J., and Montpetit, B.: C-and L-band SAR signatures of Arctic sea ice during freeze-up, Remote Sensing of Environment, 279, 113 129, 2022.

Mäkynen, M. and Karvonen, J.: Incidence angle dependence of first-year sea ice backscattering coefficient in Sentinel-1 SAR imagery over the Kara Sea, IEEE Transactions on Geoscience and Remote Sensing, 55, 6170–6181, 2017.

Matthews, B. W.: Comparison of the predicted and observed secondary structure of T4 phage lysozyme, Biochimica et Biophysica Acta (BBA)-Protein Structure, 405, 442–451, 1975.

Melsheimer, C. and Spreen, G.: AMSR2 ASI sea ice concentration data, Arctic, version 5.4 (NetCDF)(July 2012-December 2019), (No Title), 2019.

Onstott, R. and Gogineni, S.: Active microwave measurements of Arctic sea ice under summer conditions, Journal of Geophysical Research: Oceans, 90, 5035–5044, 1985.

Radhakrishnan, K., Scott, K. A., and Clausi, D. A.: Sea ice concentration estimation: Using passive microwave and SAR data with a U-net and curriculum learning, IEEE Journal of Selected Topics in Applied Earth Observations and Remote Sensing, 14, 5339–5351, 2021.

Rusin, J., Doulgeris, A. P., Scott, K. A., Lavergne, T., and Taelman, C.: High Resolution Sea Ice Concentration Using a Sentinel-1 U-Net Ice-Water Classifier, IEEE Journal of Selected Topics in Applied Earth Observations and Remote Sensing, 2025.

https://doi.org/10.5194/egusphere-2026-4775
Preprint. Discussion started: 21 August 2026

Rusin, J., Doulgeris, A. P., Lavergne, T., Scott, K. A., and Dinessen, F.: Towards Higher Resolution Arctic Winter Sea Ice Concentration: Addressing Sentinel-1 Misclassification With AMSR2 Data Fusion, IEEE Journal of Selected Topics in Applied Earth Observations and Remote Sensing, 2026.

Schyberg, H., Yang, X., Køltzow, M. A. Ø., Amstrup, B., Bakketun, Å., Bazile, E., Bojarova, J., Box, J. E., Dahlgren, P., Hagelin, S., Homleid, M., Horányi, A., Høyer, J., Johansson, Å., Killie, M. A., Körnich, H., Le Moigne, P., Lindskog, M., Manninen, T., Nielsen Englyst, P., Nielsen, K. P., Olsson, E., Palmason, B., Peralta Aros, C., Randriamampianina, R., Samuelsson, P., Stappers, R., Støylen, E., Thorsteinsson, S., Valkonen, T., and Wang, Z. Q.: Arctic regional reanalysis on single levels from 1991 to present, https://doi.org/10.24381/cds.713858f6, accessed on 13-06-2025, 2020.

Spreen, G., Kaleschke, L., and Heygster, G.: Sea ice remote sensing using AMSR-E 89-GHz channels, Journal of Geophysical Research: Oceans, 113, 2008.

Wakabayashi, H. and Sakai, S.: Estimation of sea ice concentration in the Sea of Okhotsk using PALSAR polarimetric data, in: 2010 IEEE International Geoscience and Remote Sensing Symposium, pp. 2398–2401, IEEE, 2010.

Wakabayashi, H., Matsuoka, T., Nakamura, K., and Nishio, F.: Polarimetric characteristics of sea ice in the Sea of Okhotsk observed by airborne L-band SAR, IEEE Transactions on Geoscience and Remote Sensing, 42, 2412–2425, 2004.

Wang, L. and Scott, K.A.and Clausi, D.: Sea Ice Concentration Estimation during Freeze-Up from SAR Imagery Using a Convolutional Neural Network, Remote Sensing, 9, 408, 2017.

Wang, L., Scott, K., Xu, L., and Clausi, D.: Sea ice concentration estimation during melt from dual-pol SAR scenes using deep convolutional neural networks: A case study, IEEE Trans. Geosci. Remote Sens., 54, 4524–4533, 2016.

Wang, Q., Lohse, J. P., Doulgeris, A. P., and Eltoft, T.: Data augmentation for SAR sea ice and water classification based on per-class backscatter variation with incidence angle, IEEE Transactions on Geoscience and Remote Sensing, 61, 1–15, 2023.

Wu, S., Yang, S., and Kou, S.: Are Statistical Methods Obsolete in the Era of Deep Learning? A Study of ODE Inverse Problems, The American Statistician, pp. 1–16, 2026.

Wulf, T., Buus-Hinkler, J., Singha, S., Shi, H., and Kreiner, M. B.: Pan-Arctic sea ice concentration from SAR and passive microwave, The Cryosphere, 18, 5277–5300, 2024.

Wulf, T., Buus-Hinkler, J., Singha, S., Dasgupta, N., Athanasiadis, A., and Kreiner, M. B.: A decade of sea ice concentration retrieved from sentinel-1, Remote Sensing of Environment, 337, 115 252, 2026.